Tuning the topological character of half-Heusler systems: A comparative study on $YTBi$ (T = Pd, Pt)

J. C. Souza,[1,2,*] M. V. Ale Crivillero,[2] H. Dawczak-Dębicki,[2] Andrzej Ptok,[3] P. G. Pagliuso,[1,4] and S. Wirth[2,†]

[1]*Instituto de Física "Gleb Wataghin," Universidade Estadual de Campinas (UNICAMP), 13083-859 Campinas, SP, Brazil*

[2]*Max Planck Institute for Chemical Physics of Solids, D-01187 Dresden, Germany*

[3]*Institute of Nuclear Physics, Polish Academy of Sciences, W. E. Radzikowskiego 152, PL-31342 Kraków, Poland*

[4]*Los Alamos National Laboratory, Los Alamos, New Mexico 87545, USA*

(Received 24 July 2023; accepted 16 October 2023; published 31 October 2023)

Half-Heusler systems host a plethora of different ground states, especially with nontrivial topology. However, there is still a lack of spectroscopic insight into the corresponding band inversion in this family. In this work, we locally explore the half-Heuslers $YTBi$ (T = Pt and Pd) by means of scanning tunneling microscopy/spectroscopy. From our analysis of the (120) surface plane, we infer that the increase of the spin-orbit coupling upon going from Pd to Pt is the main player in tuning the surface states from trivial to topologically nontrivial. Our measurements unveil a (2×1) reconstruction of the (120) surface of both systems. Using density functional theory calculations, we show that the observed different behavior of the local density of states near the Fermi level in these two materials is directly related to the presence of metallic surface states. Our work sheds new light on a well known tunable family of materials and opens new routes to explore the presence of topological states of matter in half-Heusler systems and its microscopic observation.

DOI: 10.1103/PhysRevB.108.165154

I. INTRODUCTION

The seminal works on the quantum (spin) Hall effect [1–3] were crucial to definitely incorporate topology into the analysis of electronic band structure of solids [4–6]. The net result was the prediction and observation of a plethora of quantum topological states of matter, such as topological insulators (TIs) [6], Dirac and Weyl semimetals [5,7], and even more exotic excitations [8,9]. Due to its unique physical properties, in which surface states often play a decisive role [5,6], the application of such systems can reach from spintronics to quantum computing [10].

Despite such potential applications, two key ingredients have been limiting factors for a broader use of TIs [10,11]. The first one is that many materials have their Fermi energy E_F located in one of the bands derived from the bulk. In other words, experimentally the bulk is not fully insulating, as, e.g., typically observed in layered chalcogenides [11–14]. Secondly, the Dirac point is often located sizeably away from E_F, preventing these materials from potential usage in, e.g., transport applications. A solution for both problems may reside in correlated systems, where the many-body interactions pin the Dirac point close to E_F, within the bulk gap [15,16]. However, their correlated phases normally appear only at low temperatures, which implies that those topological phases may not be suitable for applications [17–21]. As such, it is imperative to find appropriate materials with an insulating-like bulk and Dirac points near E_F, whose properties can also be tuned to specific requirements and even show a good match to important semiconducting substrates [22].

One of the most versatile systems that host numerous topological states of matter is the half-Heusler compounds [4,23]. This family, with a simple MgAgAs-type cubic structure (space group $F\bar{4}3m$), that can be seen as a ZnS-type structure with filled octahedral lattice sites [Fig. 1(a)] [23], has been extensively explored due to the fact that its semiconducting, magnetic, thermoelectric, and strongly correlated properties can often be tailored [4,24–28]. Earlier theoretical calculations have suggested that the mechanism behind the appearance of topological features in this family depends on the band inversion, which is very similar to that observed in the prototypical CdTe and HgTe systems [29]. In both compounds, at the Γ point near E_F, the energy bands are split into Γ_6, Γ_7 (both twofold degenerate), and Γ_8 (fourfold degenerate) states. This splitting originates from the zinc blende crystal symmetry and strong spin-orbit coupling [29–32]. In the context of band topology, CdTe possesses a normal band order (the s-like Γ_6 state sits above the p-like Γ_8 state), while in the HgTe band, inversion occurs such that Γ_6 resides below Γ_8 [33]. Both situations are reproduced in $YTBi$, where for T = Pd the normal (trivial) state is realized, while for T = Pt a band inversion occurs and nontrivial states emerge (see Fig. 9 in the Appendix) [29–32].

In fact, previous angle-resolved photoemission spectroscopy (ARPES) measurements on YPtBi have shown the

*Current address: Department of Condensed Matter Physics, Weizmann Institute of Science, Rehovot, Israel.

†steffen.wirth@cpfs.mpg.de

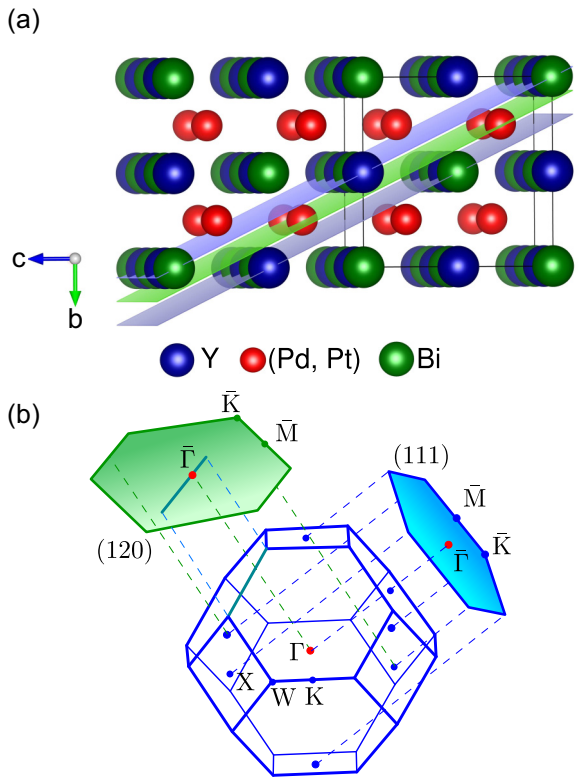

FIG. 1. (a) Crystal structure of the half-Heusler systems. The blue and green planes indicate the (120) planes of YBi and Pd/Pt termination, respectively. The black lines outline the unit cell. (b) Brillouin zone and its projection for the (111) and (120) surface planes.

presence of unusual topological surface states [34,35]. Here, the topological surface states are observed throughout the Brillouin zone. This situation is different from the one typically observed, e.g., in the chalcogenides TIs, where the topological surface states emerge as a Dirac cone [33,34,36,37]. Moreover, topological features were also observed in the form of Weyl fermions in related half-Heusler semimetals *R*PtBi (*R* = Nd, Gd, Yb) [17,38,39]. In particular, topological features can affect a possible superconducting state, even resulting in triplet superconductivity for some members of the *RT*Bi family (R = rare earth, T = Pd or Pt) [40–46].

In an even more fundamental aspect, comparing YPtBi and YPdBi can be an excellent platform to experimentally tune the topological properties through the spin-orbit coupling. Both systems possess very similar lattice parameters [6.652(1) and 6.639(1) Å for YPtBi [41] and YPdBi [42], respectively], which makes the spin-orbit coupling the key parameter to distinguish between trivial (YPdBi) and nontrivial (YPtBi) topological states [30–32,34,35]. These compounds are particularly attractive due to the possibility of obtaining high-quality thin films, increasing their potential applicability [47]. Previous nuclear magnetic resonance (NMR) [48,49] and electron spin resonance (ESR) experiments [50] pointed toward a strong impact of spin-orbit coupling on the detailed band structure of *YT*Bi. A direct experimental visualization of the surface states resulting from band inversion in half-Heuslers has not been demonstrated, yet.

Additionally, although this family of materials supports so many different physical properties, which are often related to surface states, little is known about the surface properties of half-Heuslers. This is, at least in part, certainly related to the fact that half-Heusler compounds with cubic structure are notoriously difficult to cleave, rendering an *in situ* preparation of atomically flat surfaces from bulk samples a challenge. As a consequence, reports employing scanning tunneling microscopy/spectroscopy (STM/STS) are scarce and focused on disordered surfaces in single crystals [51] or on the study of surface reconstructions in thin films [52]. In this work, we report on atomically flat surfaces investigated by STM/STS, combined with first-principles density functional theory (DFT) slab calculations, to explore the local properties of the half-Heuslers YPdBi and YPtBi. We cleaved our samples *in situ*, most likely along the (120) planes exposing a (2×1) reconstructed YBi-terminated surface. From our STS data we infer a *finite* local density of states (local DOS or LDOS) $\eta(E)$ at E_F for YPtBi, while the trivial YPdBi compound exhibits a well-defined gap around E_F. We argue that the difference in the LDOS is likely due to the formation of metallic surface states in YPtBi, a finding corroborated by our slab calculations. Our work establishes the possibility of using STM as a local probe to investigate half-Heusler systems, and it suggests that a tuning of the LDOS can be achieved through the increase of the spin-orbit coupling upon going from Pd to Pt.

II. METHODS

Single crystalline samples of Y(Pd,Pt)Bi were synthesized by the Bi self-flux growth technique with starting elements Y (99.99%):(Pd,Pt) (99.99%):Bi (99.999+%) in the proportion of 1:1:10 [53]. While YPtBi samples naturally expose (001), (110), and (111) planes in a pyramidlike shape, YPdBi samples only expose (001) planes (all samples had a cubelike shape). The investigated samples had an approximate size of $1 \times 1 \times 1$ mm^3.

STM/STS measurements were performed in an ultrahigh-vacuum system at pressures $p \leqslant 2.5 \times 10^{-9}$ Pa and at temperatures $T = 4.6$ K. A total of seven (four YPdBi and three YPtBi) samples were cleaved *in situ* at temperatures $T \approx 20$ K. The tunneling current I was measured using electrochemical prepared tungsten tips, and a bias voltage V_b was applied to the samples. The topographies were obtained in a constant current mode with a predefined current set point I_{sp}. Most topographies were obtained in a dual-bias mode, i.e., forward and backward scans along the fast scan direction were obtained with a V_b of the same magnitude, but with opposite signs. We did not see any differences in dual-bias mode (i.e., for the different values of V_b) when scanning the samples along the (120) planes. The dI/dV spectra were acquired by a lock-in technique applying a modulation voltage of typically $V_{mod} = 0.3$ mV at 117 Hz.

The first-principles density functional theory (DFT) calculations were performed using the projector augmented-wave (PAW) potentials [54] implemented in the Vienna Ab initio Simulation Package (VASP) code [55–57]. The calculations containing the spin-orbit coupling (SOC) were performed with the generalized gradient approximation (GGA) under the

modified Becke-Johnson (mBJ) exchange potential [58–60]. The energy cutoff for the plane-wave expansion is set to 350 eV. The density of states was calculated using $12 \times 12 \times 12$ **k**-point Γ-centered grids in the Monkhorst-Pack scheme [61]. The lattice constants were assumed to be equal to the experimental values, i.e., $\approx$ 6.64 Å for both compounds [62]. The band structures from the DFT calculations were used to find tight-binding models by WANNIER90 [63,64], which allowed us to calculate surface-state spectra by WANNIERTOOLS [65]. The theoretical simulations of STM topographies for (120) YBi-terminated surfaces (without and with reconstruction) were computed using the Tersoff-Hamann approach [66]. Due to technical limitations of the mBJ potential for slab-type calculations, these specific DFT calculations were performed using a GGA with Perdew-Burke-Ernzerhof (PBE) parametrization [67]. More details on the calculations are provided in Appendix D.

III. RESULTS AND DISCUSSION

A. Topography of YPtBi single crystals

In situ preparation of clean surfaces (in the case of bulk single crystals typically by cleaving) is of utmost importance for STM/STS studies but often exceedingly difficult for materials of cubic crystal structure [20]. Our single crystals of half-Heusler compounds YPdBi and YPtBi naturally expose (001) crystallographic planes, while the (111) plane was only found for YPtBi. Figure 1(b) shows the surface projection of the Brillouin zone along the latter direction. In principle, the pyramid-like shape of our YPtBi samples may open the possibility of exploring surfaces along the (001) and (111) planes. However, the YPdBi crystals had a more cubelike shape, suggesting a preferred cleave along the (001) plane. We emphasize that for a reasonable comparison between results obtained on both compounds, it is vital to investigate *identical* crystallographic planes. Therefore, we focus on samples mounted along the (001) direction in the following [further details of measurements for cleaving YPtBi along the (111) plane are provided in Appendix A; see Figs. 4, 5, and 6].

Atomically flat surfaces on cleaved half-Heuslers are extremely scarce and required extensive search. One example is shown in Fig. 2(a) for YPtBi where, in principle, the cleaving was expected to occur along the (001) plane. Before comparing the results from two different compounds, it is crucial to identify which planes and terminations are obtained since surface states depend decisively on those two parameters [34,35]. Notably, all the obtained flat surfaces show a $\sim 30^\circ$ tilt angle with respect to the sample mounting plane (001) in this cleaving configuration. This is a hint that the obtained surfaces are *not* (001) planes. As will be argued below, the exposed planes are likely YBi-terminated (120) planes instead, which are highlighted in blue in Fig. 1(a).

Three crucial pieces of information are helpful to identify the cleaving plane: (i) As mentioned, the surfaces are tilted by $\sim 30^\circ$ with respect to the sample mounting plane. This renders the (120) plane a likely surface as it is expected 26.6° away from the (001) plane. (ii) The distance between corrugations and (iii) the height of the step edges can be analyzed. Figure 2(a) exemplifies the latter two in the same field of view. The apparent height profile Δz as a function of the lateral distance Δx (height scans) shown in Fig. 2(b) reveals a step edge height of $\sim$115 pm and a distance between corrugations $d_{\mathrm{exp}}^{(120)\mathrm{Pt}} = 0.66(3)$ and 0.68(3) nm for the pink and turquoise directions, respectively. Those distances are in agreement with the ones extracted from the Fourier transform of larger areas, from which we obtain $d_{\mathrm{exp}}^{(120)\mathrm{PtFT}} = 0.67(3)$ and 0.70(3) nm (see Fig. 7 in the Appendix).

To gain better statistics on the average step edge height, a $100 \times 100\mathrm{nm}^2$ area obtained on YPtBi is investigated; see Fig. 2(c). We can clearly see the occurrence of several step edges and a lack of adatoms. We note that the latter observation distinguishes the surfaces observed here over measurements on the (111) plane (compare Fig. 4 in the Appendix). The average step edge height between different exposed surfaces is $d_{\mathrm{exp}}^{(120)} \approx 135$ pm [Fig. 2(d)] indicating that either exclusively YBi-terminated or Pt-terminated surfaces are observed. Note that the theoretically expected distance between these planes is 148 pm; see Fig. 1(a). A Pt-terminated surface can be ruled out since a distorted hexagonal lattice with distances between Pt atoms of 0.66 and 0.81 nm would be expected, Fig. 2(h), which is in clear contrast to the observation of Fig. 2(a). On the other hand, for a YBi-terminated surface, a rectangular lattice with distances of 0.33 and 0.74 nm between atoms is expected. Therefore, we propose a (2×1) reconstructed YBi surface where half of the atoms are missing; see Fig. 2(i). This scenario is consistent with the observed distances between corrugations and STM simulations obtained through slab DFT calculations.

Reconstructed surfaces, including the (2×1) type, are commonly observed on both bulk samples [52] and thin films [68–71] of half-Heusler compounds. The driving forces behind these reconstructions were argued to be charge neutrality and a minimization of the number of dangling bonds [34,35,52]. However, the (120) surface plane has not been investigated so far. To get further insight, we conducted first-principles slab calculations for this particular surface termination. Specifically, the total energies for slabs without and with (2×1) reconstruction were calculated. The reconstructed slabs contained 84 sites, i.e., 28 atoms of each species (for further details, see Appendix D). To allow comparison to the nonreconstructed surface, two Pd/Pt atoms were removed from one surface, but added as free atoms to the total energies. The calculations clearly favor a reconstructed surface by about 4.1 eV in the case of YPdBi, and about 8.3 eV for YPtBi.

From the valence situation in the half-Heusler compounds, one may expect a YBi-terminated surface to be charge-neutral. In line with the statement above [52], one may then speculate about a minimum number of dangling bonds for the reconstructed surface and hence a limited impact of dangling bonds on the surface properties.

B. Topography of YPdBi

Naturally, also on YPdBi, atomically flat surfaces needed to be searched for extensively. Areas of 30×30 nm^2 could be identified, as exhibited in Fig. 2(e). However, we were not able to find any step edges in all of our investigated YPdBi cleaves. Importantly, within these areas we observed the same rectangular pattern as for YPtBi. This pattern is

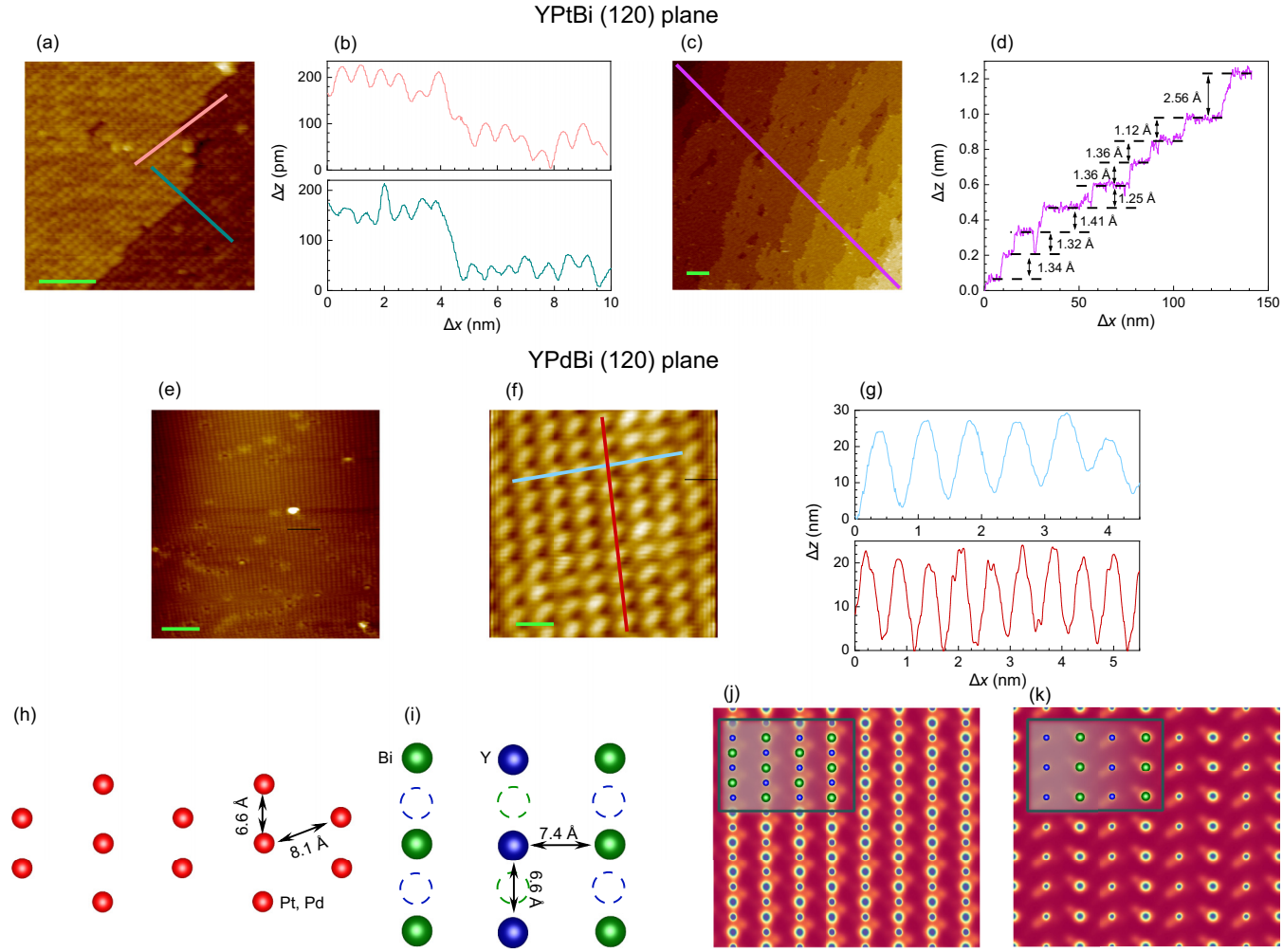

FIG. 2. (a) 20×20 nm^2 topography along the (120) plane for YPtBi (bias voltage $V_b = -300$ mV, $I_{sp} = 0.7$ nA, scale bar of 5 nm). The height scans along two (almost) perpendicular directions are shown in (b) by curves of corresponding color. The step edge height is, approximately, 115 pm. (c) 100×100 nm^2 field of view (scale bar of 10 nm). The height scan along the violet line over several step edges is presented in (d). (e) 30×30 nm^2 STM topography along the (120) plane for YPdBi ($V_b = -200$ mV, $I_{sp} = 0.6$ nA, scale bar of 5 nm). (f) High-resolution 6×6 nm^2 field of view (scale bar of 1 nm). (f) Two perpendicular height scans from (f) are presented by corresponding colors. View onto the topmost layer of (h) Pd/Pt- and (i) YBi-terminated surfaces for the (120) plane. In (i), the proposed (2×1) surface reconstruction is indicated, where hollow circles mark empty atom positions. Theoretically predicted STM topography for (120) surfaces: (j) unreconstructed and (k) (2×1) reconstructed YBi-terminated surface. The topography was simulated for a tip $\sim$1 Å above the surface of area 5.3×5.9 nm^2. The blue (red) corresponds to high (low) charge density.

confirmed by high-resolution topographies, as presented in Fig. 2(f), where the obtained distances between corrugations are $d_{\text{exp}}^{(120)\text{Pd}} = 0.61(3)$ and 0.72(3) nm [Fig. 2(g)]. These values are consistent with results from Fourier analyses obtained on bigger areas (see Fig. 7 in the Appendix) as well as with the YPtBi results.

Apart from the missing step edges, all of the investigated, atomically flat areas on YPdBi appeared to be consistent with the plane orientation and termination as observed for YPtBi cleaves. In particular, the experimentally obtained surfaces are again tilted by $\sim 30^\circ$ with respect to the sample mounting plane (001). Hence, our observations point again toward (2×1) reconstructed surfaces along the (120) plane.

Figures 2(j) and 2(k) represent STM simulations obtained through slab DFT calculations for YBi-terminated surfaces without and with (2×1) reconstruction, respectively (for details, see Appendix D 3). These results indicate that without a surface reconstruction we would likely observe stripes along the (100) crystallographic direction [Fig. 2(j)]. Such stripes are absent on (2×1) reconstructed surfaces [Fig. 2(k)], in line with our observations.

The simulations also help to explain the subtle differences in the topographies upon going from Pd to Pt samples. For a (120) termination, the Pd/Pt atoms reside only 74 pm below the topmost YBi layer, and hence the Pd/Pt atoms may also contribute to the topography, as suggested by the yellow contributions in Figs. 2(j) and 2(k). The radial extent of the $4d$ orbitals is smaller than the $5d$ ones [72,73]. Therefore, the second-to-topmost layer may have slightly different contributions to the topography depending on whether it is Pd or Pt.

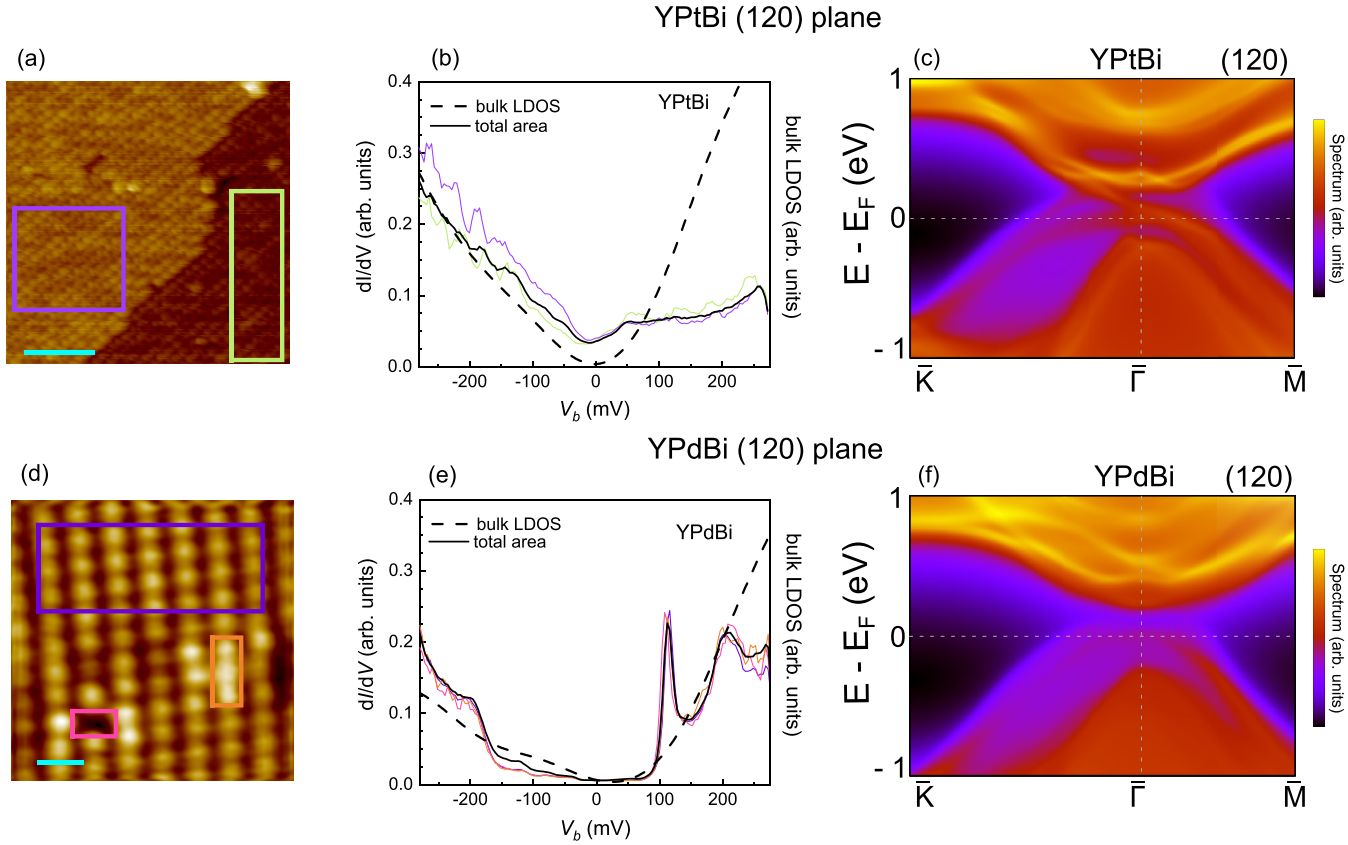

FIG. 3. (a) Topography of YPtBi as in Fig. 2(a) with areas marked within which dI/dV spectra were averaged (in addition to the total area). (b) dI/dV spectra within the purple and green rectangles as well as for the total area (black) presented in (a). Also, the calculated bulk DOS (dashed line) is included. The latter is normalized at negative bias to the experimental value to improve the visualization. (c) Slab calculated electronic band structure for a YBi-terminated (120) plane of YPtBi. (d) 6×6 nm^2 topography for YPdBi ($V_b = -200$ mV, $I_{sp} = 0.6$ nA, scale bar of 1 nm). (e) dI/dV spectra averaged over the magenta, orange, purple, and the whole area shown in (d). Again, the calculated bulk DOS for YPdBi is included for comparison (dashed line). (f) Slab calculated electronic band structure for the YBi-terminated (120) plane of YPdBi.

C. Bulk properties of Y*T*Bi (*T* = Pd, Pt)

Before discussing our spectroscopic results of the *surface* properties of YPdBi and YPtBi, we address possible differences in the *bulk* DOS near E_F for these two materials as this may easily influence the spectral weight measured at the surface.

As already mentioned, half-Heusler systems have a three-dimensional character, and, as such, bulk states might be relevant [74,75]. In fact, previous specific-heat studies have obtained very similar Sommerfeld coefficients γ for both systems. While for YPdBi $\gamma = 0.3(1)$ mJ mol^{-1}K^{-2} was reported [53], results for YPtBi ranged from ∼0.1 to 0.4 mJ mol^{-1}K^{-2} [43,76]. Assuming a free conduction electron gas model with $\gamma = (2/3)\pi k_B^2 \eta_s(E_F)$, where k_B is the Bohr magneton and $\eta_s(E_F)$ denotes the spin-resolved DOS at E_F, one obtains $\eta_s(E_F)^{\mathrm{YPdBi}} = 0.06(4)$ eV^{-1} mol^{-1} spin^{-1} for YPdBi, and $\eta_s(E_F)^{\mathrm{YPtBi}} = 0.04(4)$ eV^{-1} mol^{-1} spin^{-1} for YPtBi. Such a negligible electronic contribution to the specific heat is consistent with previous transport measurements for both systems, which reported a semiconductor/semimetal-like behavior [41–44,53,76–78].

It is worth noting that Pd/Pt and Bi-based compounds are known for hosting impurity phases, such as Bi and/or Pd/Pt-Bi binary phases [73]. Such impurity phases may affect the macroscopic properties, especially transport measurements. Consequently, it is highly desirable to have an experimental confirmation of the insulating bulk nature from a microscopic technique. Indeed, previous electron spin resonance measurements for rare-earth substituted YPdBi and YPtBi clearly indicate an insulating bulk behavior. This establishes the presence of a small gap in the bulk DOS at E_F of both systems [53,76], in agreement with our DFT results discussed below.

D. Spectroscopic results on Y*T*Bi (*T* = Pd,Pt)

Having identified identical surface terminations and established negligible bulk contributions to the DOS near E_F for both materials YPdBi and YPtBi, we can now compare their surface electronic properties. In Figs. 3(b) and 3(e) the STS results, i.e., dI/dV spectra, are presented. We note that, within simplifying assumptions, $dI/dV \propto \eta(E)$. The topographic areas over which the spectroscopy curves were averaged are shown in Figs. 3(a) and 3(d), respectively, with the black curves in (b) and (e) obtained within the total areas of (a) and (d). Clearly, there are only minor differences between spectra obtained in different areas of a given compound. In particular, for YPdBi also spectra obtained at different defects are included [see the orange and pink rectangles/curves in Figs. 3(d) and 3(e)], which do not significantly deviate from

the spectra in a clean (violet) or the total area. Consequently, the spectra are not significantly influenced by these defects.

The dI/dV spectra of YPtBi are mostly featureless, with a V-like shape near E_F and a minimum at around -10 meV. Most importantly, we obtain a finite LDOS around E_F, which is a clear indication for a considerable amount of surface states closing the bulk gap.

This experimental result is to be contrasted with the bulk DOS as calculated by DFT [black dashed line in Fig. 3(b) and Fig. 9(b)], which predicts a gaplike behavior near E_F. The calculations also find a mostly featureless spectrum and, for negative bias away from E_F, qualitatively agree with our dI/dV data. However, a proper analysis, and specifically insight into the details near E_F, requires a slab calculation, the result of which is put forward in Fig. 3(c). The calculations were conducted with the Green function technique for semi-infinite systems assuming a (120) surface representing our experiments in a more realistic way. As discussed in Appendix D 3, with the modified Becke-Johnson (mBJ) pseudopotential [58–60], it is not possible to perform slab calculations using reconstructed surfaces or to obtain the LDOS properly. Nonetheless, we are able to obtain important pieces of information to understand our STS results. As shown in Fig. 3(c), a mixture of surface states (nontrivial and trivial ones) contributes significantly to the spectral weight within the bulk gap, which is consistent with previous angle-resolved photoemission spectroscopy results [34,35]. In other words, surface states dominate the LDOS near E_F, which clearly indicates that the increase of the LDOS in YPtBi, compared to the bulk DOS, stems directly from those surface states. As shown in Fig. 3(c), near the Γ point at $\sim$300 meV we obtain a high surface spectral weight of dangling bonds. Those trivial surface states are very similar to the van Hove singularity at approximately -100 meV that is found for LuPtBi [31,79,80].

The results of our dI/dV measurements for YPtBi become even more intriguing when compared to those of YPdBi, Fig. 3(e). There are two striking distinctions in the dI/dV data of YPdBi: (i) Qualitatively, the LDOS exhibits more features, with a prominent peak at approximately 115 meV. (ii) Importantly, there is a clearly observable gap of width $\Delta \sim 100$ meV around E_F. We should note, however, that the dI/dV data for YPdBi do not strictly go all the way to zero, but remain finite at a very small value, possibly caused by thermal effects.

A comparison of the experimental data with the calculated bulk DOS is only partially possible, Fig. 3(e). On the one hand, the band gap $\Delta^{\text{theor}} \sim 0.15$ eV [see Fig. 9(a)] in the projection to the (120) plane is comparable to the experimental value. This gap once again confirms the trivial nature of YPdBi, in which the conduction and valence bands are not inverted. Moreover, there appear to be no surface states near E_F in this case. Most of the spectral weight coming from surface states is located above E_F, which is consistent with our dI/dV being almost featureless at negative bias.

E. Comparison between YPtBi and YPdBi

The differences observed in the dI/dV spectra of YPtBi and YPdBi are intriguing given the facts that identical surface terminations were investigated (thereby ruling out the surface reconstruction as the main cause of the differences), and both compounds have very small bulk contributions to the DOS near E_F. The slab calculated electronic band structures for the YBi-terminated (120) surface plane, Figs. 3(c) and 3(f), suggest a considerable admixture of nontrivial surface states to the DOS near E_F in case of the YPtBi surface, which is absent for YPdBi. In such a case, it is a likely scenario that the topological surface states are the key component for the differences in the dI/dV spectra near E_F. The minimum observed close to $V_b \sim -10$ meV in the case of YPtBi may then be linked to the Dirac point.

It is also interesting to note that the peaklike feature at $V_b = +115$ meV is only observed for YPdBi. Two different origins could be at play to cause this peak. In the first scenario, which is suggested by our slab calculations, this feature coincides with the bottom of the conduction band, as shown in Fig. 3(f) and discussed in Appendix D 3 and Fig. 12. Here, the lack of this peak for YPtBi could naturally be explained by the band inversion in this compound. As discussed in the Introduction, nontrivial surface states emerge thereupon.

An alternative scenario involves the presence of the surface reconstruction. Here, the peak would be a direct consequence of the enhancement of trivial surface states. However, in this scenario one should also expect such a peak for YPtBi, which is not observed experimentally. We emphasize that such a comparison is only possible since results obtained on *identical* surface terminations (concerning the type and arrangement of the surface atoms as well as the orientation of the terminating plane) are compared. The clear difference between the LDOS of both systems near E_F favors the increased spin-orbit coupling (upon going from Pd to Pt) as the source of the appearance of surface states with topological character. The predicted, strong modification of these surface states, to the best of our knowledge, has not been demonstrated by STM/S before and suggests a systematic tunability of topology in half-Heusler systems. Likely, by choosing the proper surface plane, these properties also may be accessed through macroscopic (e.g., transport) measurements.

Finally, our results, even though they were obtained at $T = 4.6$ K, may also shed some light on superconductivity in half-Heusler systems. A well-defined gap was found for the trivial insulator YPdBi. This compound has been reported to have one of the highest superconducting transition temperatures ($T_c \sim 1.6$ K) among the *R*PdBi family [44]. If the superconductivity is intrinsic, it would be interesting to understand how a gapped system can develop a superconducting phase. In this respect, it is interesting to note that, at least for YPtBi, some reports discuss the possibility of superconductivity being a bulk or a surface property [41,47]. Yet, a finite LDOS, possibly with Dirac point(s), for YPtBi is not inconsistent with a topological superconductivity scenario [40–43,45–47,81]. It would be interesting to conduct further experiments at mK temperatures to investigate the origin of superconductivity and its nature in half-Heusler systems.

IV. CONCLUSION

In summary, we performed scanning tunneling microscopy/spectroscopy on the half-Heusler systems

YPtBi and YPdBi. By *in situ* cleaving the single crystals at low temperatures, we were able to investigate atomically flat areas. Both materials very likely expose (120) YBi-terminated surfaces with (2×1) reconstructions, which induce additional surface states and hence may complicate surface spectroscopy. Using STM, we can compare *identical* surface terminations, thereby ruling out the reconstructions as the main cause for differences in the spectroscopic results between the two materials. However, we do observe a clear difference in the LDOS of these compounds: While YPdBi exhibits a gap of ∼100 meV around E_F, surface states are found for YPtBi without indication of a gap. Such distinct behavior was not seen by macroscopic measurements reported in previous studies. Our result provides evidence for the targeted realization of unusual surface states. DFT calculations are consistent with such a change in the LDOS.

In a more general way, our result can very likely be linked to a spin-orbit tuning of topology in half-Heusler systems. More importantly, our results emphasize the key role of surface states near E_F in these systems. Exploring planes such as the (120) surface termination [or even the (001) plane in thin films] appears to be an extremely promising route to obtain a versatile TI with an insulating bulk, and it increases the potential of half-Heusler systems for applications.

ACKNOWLEDGMENTS

We thank E. H. da Silva Neto, T. J. Boyle, and M. Walker for their help and discussions in the beginning of this project. This work was supported by FAPESP (SP-Brazil) Grants No. 2020/12283-0, No. 2018/11364-7, and No. 2017/10581-1, CNPq Grant No. 311783/2021-0, and CAPES. Work was also supported by the National Science Centre (NCN, Poland) under Projects No. 2021/43/B/ST3/02166 (A.P.). A.P. appreciates funding within the framework of scholarships of the Minister of Science and Higher Education of Poland for outstanding young scientists (2019 edition, No. 818/STYP/14/2019). Work at Los Alamos was supported by the Los Alamos Laboratory Directed Research and Development program through Project No. 20210064DR.

APPENDIX A: (111) PLANE IN YPtBi

1. STM/STS results

In YPtBi crystals with a pyramidlike shape, we are also able to cleave along the (111) plane; the results are summarized in Fig. 4. In this plane, the height difference between Y and Bi layers is twice as large as the Y-Pt or Pt-Bi layer spacing; see Fig. 4(a). Furthermore, fewer chemical bonds need to be broken between Y and Bi layers compared to cleaves involving Pt layers, which should result in cleaves

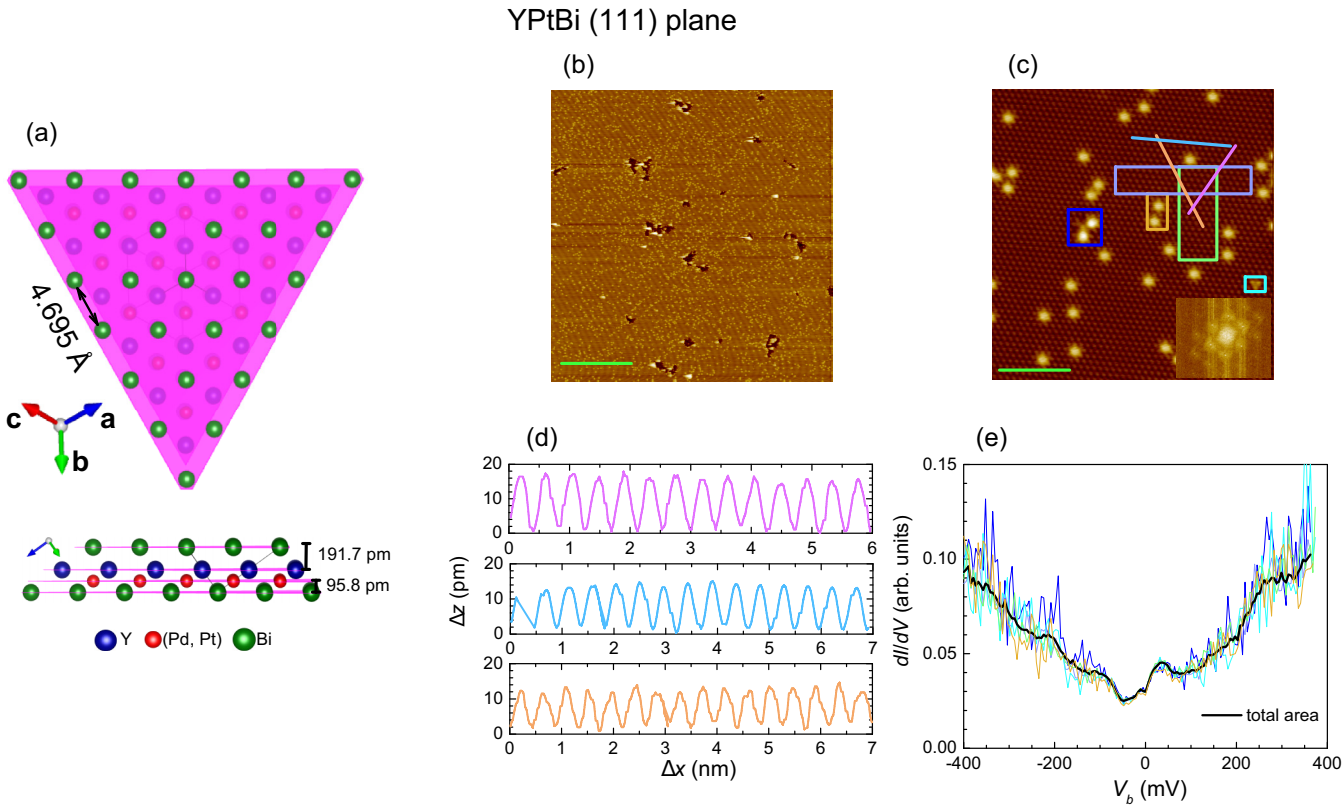

FIG. 4. (a) The triangular lattice of the (111) plane of the half-Heusler systems and the height difference between distinct termination planes. (b) 200×200 nm^2 STM topography of the (111) plane of YPtBi ($V_b = -300$ mV, $I_{sp} = 0.6$ nA, scale bar of 50 nm). (c) Atomically resolved 20×20 nm^2 topography on YPtBi along the (111) surface (scale bar 5 nm). The lower right inset shows the Fourier transform. The magenta, blue, and orange solid lines represent the direction of the height scans presented in (d). (e) dI/dV spectra averaged over the rectangular areas of corresponding colors as well as over the total field of view in (c) [black line in (e), obtained on a 35×35 grid].

exposing mostly Y or Bi layers [34]. We found more easily atomically flat surfaces along the (111) plane when compared to the cleaves along the (120) plane for YPtBi. Yet, atomically flat surfaces needed to be extensively searched for, which is not surprising in a cubic system. Importantly, however, despite great efforts, atomically flat areas on a (111) plane could *not* be found on YPdBi, and therefore the comparison of the LDOS for both compounds was focused on the (120) plane.

The cleave along the (111) plane should expose either Y- or Bi-terminated triangular lattices, as shown in Fig. 4(a). Figure 4(b) exhibits a 200×200 nm^2 topography. Although we were able to locate such large atomically flat areas, there was quite an amount of adatoms on top of such surfaces. The topography in Fig. 4(c) zooms into an area of 20×20 nm^2. In this case, it is possible to observe in more detail the triangular lattice, which is confirmed by the Fourier transform presented in the lower right inset. Again, we obtain a moderate amount of adatoms, which are expected on an unreconstructed surface due to its polar nature. The establishment of an unreconstructed surface is further corroborated by the distance between corrugations, as highlighted in the height scans of Fig. 4(d). We obtain a distance between corrugations of $d_{\text{exp}}^{(111)} = 0.43(2)$, 0.46(2), and 0.44(2) nm for the magenta, blue, and orange lines, respectively, which is in excellent agreement with the theoretical distance between Bi/Y atoms of $d_{\text{theor}}^{(111)\text{Y/Bi}} = 0.47$ nm along the (111) plane. As we will discuss in more detail below, the exposed surface is likely an unreconstructed Bi-terminated surface.

In Fig. 4(e) we present dI/dV spectra, which were obtained within the total field of view of Fig. 4(c) (black line) as well as within the areas marked by colored rectangles (with the colors corresponding to those of the spectra). Earlier theoretical calculations indicated a Dirac point buried in the bulk DOS for either Y- or Bi-terminated surfaces, which was confirmed by angle-resolved photoemission spectroscopy [34,35]. Nonetheless, trivial Rashba-like surface states can be expected due to the presence of dangling bonds [34,52]. The observed dI/dV spectra are almost featureless, with a finite DOS at the Fermi level E_{F}. Interestingly, the LDOS obtained at two adatoms [yellow area in Fig. 4(c)] or at defects [blue area in Fig. 4(c)] does not change significantly when compared to the LDOS obtained on clean surfaces (green and purple areas and spectra) or even to the spectrum averaged over the total field of view. This is an indication that the surface states are not affected locally by small amounts of disorder.

To provide further evidence for the (111) assignment of the terminating plane observed in Fig. 4, we experimentally explored the presence of step edges and adatoms. Figure 5(a) shows a typical 100×100 nm^2 topography along the (111) plane with two step edges. As can be seen in Fig. 5(b), the height difference between each exposed surface is $h_{\text{exp}}^{(111)} \approx 370$ pm. Such a distance is consistent with either Y-Y, Bi-Bi, or Pd-Pd/Pt-Pt surface terminations for which $h_{\text{theor}}^{(111)} = 383$ pm is expected. It is worth noting that there is an accumulation of adatoms along the edges of the exposed surfaces (small peaks in the height scan), which reinforces our assumption above that such adatoms play a role in neutralization of the exposed polar surfaces.

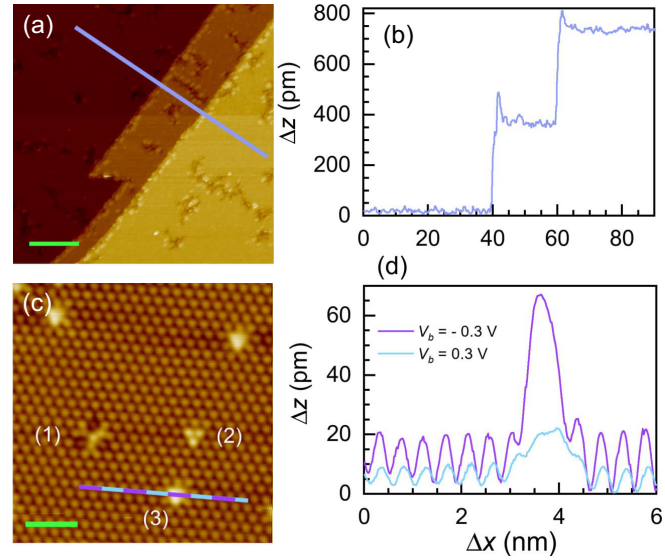

FIG. 5. (a) 100×100 nm^2 STM topography along the (111) plane of YPtBi ($V_b = 200$ mV, $I_{sp} = 0.3$ nA, scale bar of 20 nm). The purple line represents the line along which the height scan in (b) was obtained. (c) 10×10 nm^2 field of view ($V_b = -300$ mV, $I_{sp} = 0.3$ nA, scale bar of 2 nm). Here, the three most dominant defects can be recognized, which likely are a triangular vacancy [defect (1)], a triangle which could be related to a substitution [defect (2)], and adatoms [defect (3)]. The latter is supported by the violet and blue height scans in (d) obtained for opposite bias voltages along the lines indicated in (c).

Such an assumption is also corroborated by different apparent heights of the adatom if measured with different bias V_b. Figure 5(c) shows a 10×10 nm^2 topography taken with $V_b = -300$ mV. We can observe the three most numerous defects obtained on these surfaces: a triangular one likely related to a vacancy [defect (1)], a small triangle which could be related to a substitution in a sublayer underneath the exposed surface [defect (2)], and the already mentioned adatoms [defect (3)]. Figure 5(d) provides the height scan across the adatom position in Fig. 5(c) with different values of the applied V_b obtained in dual-bias mode (i.e., at exactly the same position). We systematically observe higher heights at the adatom sites for negative V_b. For negative (positive) V_b, the tip will have a positive (negative) potential with respect to the sample. In this scenario, the tip gets farther away from (closer to) the adatom if it has a more positive charge compared to the surrounding bulk. We expect a valence of 3+ for Y, while the other constituents in YPtBi should have a more negative valence. Consequently, an adatom is much more likely to be more positive than its surrounding on a Bi- or Pt-terminated surface. Since a cleave exposing Pt is unlikely from the chemical bonding situation discussed above, we speculate that we obtained a Bi-terminated surface in Fig. 5.

2. Coexistence of Pt- and Bi-terminated surfaces

As already pointed out, the majority of the YPtBi samples which successfully cleaved along the (111) plane exposed the same termination within the field of view (even when step edges were included, cf. Fig. 5). However, in one particular

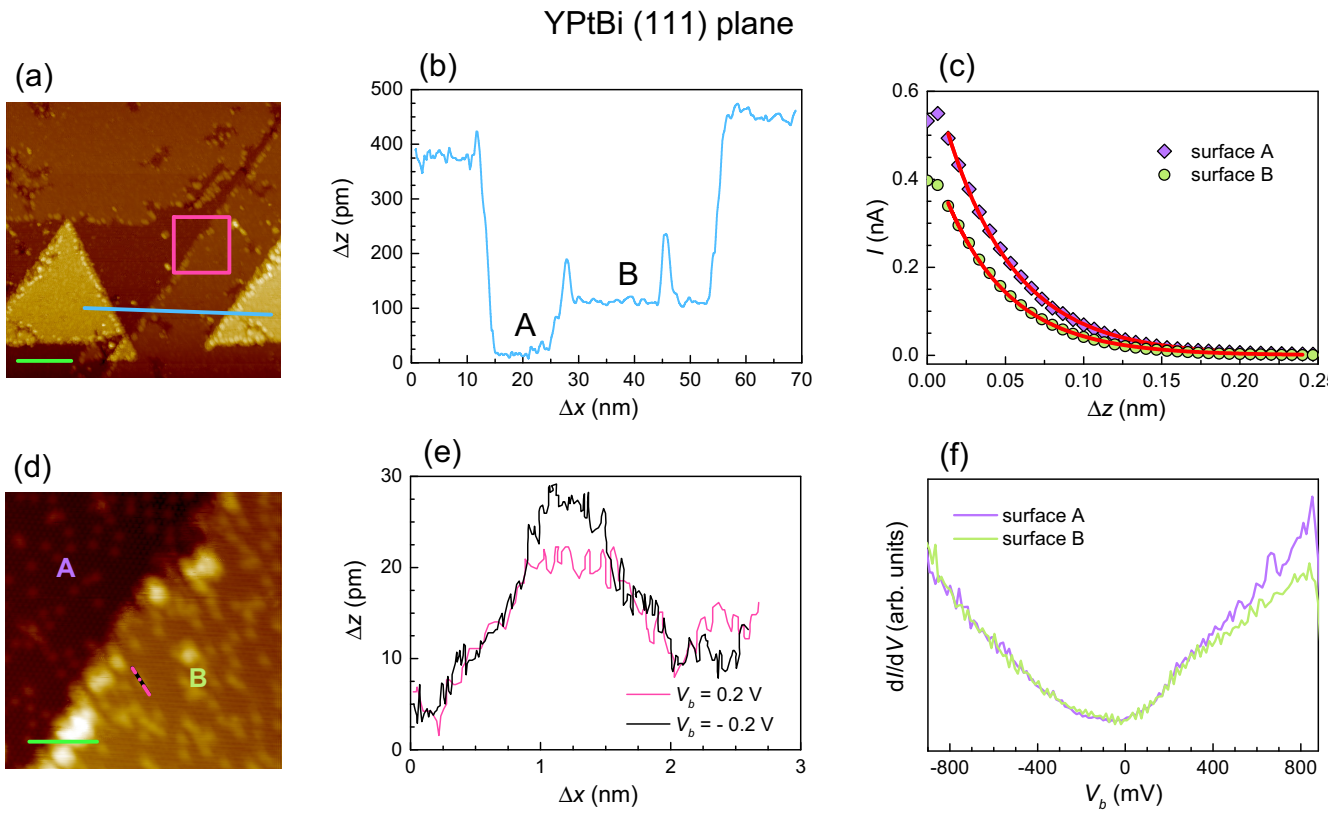

FIG. 6. (a) 100×100 nm^2 STM topography along the (111) plane for YPtBi ($V_b = -200$ mV, $I_{sp} = 0.3$ nA, scale bar of 20 nm). (b) Height scan along the blue line shown in (a). The A and B labels denote the surfaces A (Bi-terminated) and B (likely Pt-terminated). (c) Tunneling current I as a function of the tip-sample distance Δz for the two different surfaces A and B. The red solid lines are exponential fits as described in the text. (d) Zoom of 20×20 nm^2 into the magenta box shown in (a) (scale bar of 5 nm). (e) Height scan along the magenta/black line shown in (d) and for different Vb. The lines cross an adatom located in surface B. (f) Averaged dI/dV-spectra of both surfaces A and B. The averages were taken over areas of 4×4 nm^2 at equally spaced positions on 50×50 grids.

field of view we were able to observe the coexistence of two differently terminated surfaces. Figure 6(a) shows this 100×100 nm^2 topography. In the height scan explored in Fig. 6(b) we obtain a step height between two consecutive surfaces (labeled A and B) of ≈95 pm. This value is much smaller than the expected step height $h^{(111)}_{\text{theor}} = 383$ pm for identical terminations. Indeed, it is close to the Pt-Bi (or Pt-Y) layer distance, which is 95.8 pm [Fig. 4(a)]. Such a step height necessarily implies that one of the surfaces *has* to have a Pt termination.

The difference between those two surface terminations is also manifested by two different heights of the tunneling barrier Φ, which is closely related to the work function Φ_s of the sample (note that also the tip work function Φ_t enters into Φ). Φ can be obtained from an analysis of I as a function of the tip-sample distance Δz. For clean surfaces, $I(\Delta z) \propto \exp(-2\kappa\, \Delta z)$ with $\kappa^2 = 2m_e\Phi/\hbar^2$, where m_e is the bare electron mass and $V_b \ll \Phi_{s,t}$. Figure 6(c) represents $I(\Delta z)$ curves for surfaces A and B, which are identified in Figs. 6(b) and 6(d). By fitting the $I(\Delta z)$ curves [red lines in Fig. 6(c)], we obtain $\Phi_A \approx 4.9$ eV and $\Phi_B \approx 5.5$ eV. A fair comparison here is to look at the values of the elemental materials. For Y, Bi, and Pt, $\Phi_s = 3.1$, 4.22, and 5.65 eV, respectively. Comparing to our obtained results, one may speculate that the highest obtained value, i.e., Φ_B, is unlikely from a Y-terminated surface, and conversely the lower value Φ_A does not stem from a Pt-terminated surface. As one of the two surfaces (A or B) has to be Pt-terminated, it is likely surface B.

A closer look at height scans across defects can also be informative with respect to the assignment of those two distinct surfaces. A zoom into the magenta box of Fig. 6(a) is given in Fig. 6(d). According to Fig. 6(b), we identify the differently terminated surfaces as A and B in the 20×20nm^2 topography. The height scans across a defect at surface B for opposite V_b signs are shown in Fig. 6(e). They were taken at the positions highlighted by the magenta and black lines in Fig. 6(d). It is straightforward to note that the difference of the defect height for opposite V_b-values is much smaller on this surface when compared to the adatom height at surface A (which was assigned as Bi-terminated), cf. Fig. 5(d). As a consequence, the defect investigated in Fig. 6(e) is very likely located in a subsurface layer, i.e., in a layer underneath the exposed surface.

Finally, Fig. 6(f) represents dI/dV spectra as a function of V_b for both surfaces. Surprisingly, there is only a small difference at higher positive V_b-values between the spectra of the two differently terminated surfaces, suggesting that the LDOS is dominated by bulk and trivial surfaces state contributions in both cases.

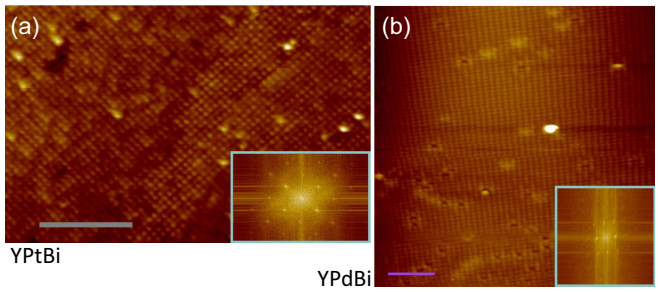

FIG. 7. (a) 25×39 nm^2 and (b) 30×30 nm^2 topographies along the (120) plane for YPtBi ($V_b = -300$ mV, $I_{sp} = 0.7$ nA, scale bar of 10 nm) and YPdBi ($V_b = -200$ mV, $I_{sp} = 0.6$ nA, scale bar of 5 nm), respectively. The right insets show the Fourier transform of the respective topography.

APPENDIX B: FOURIER TRANSFORM OF THE (120) PLANES

A more accurate extraction of the distance between corrugations can be achieved by analyzing the Fourier transform of larger areas. In the case of YPtBi, one large flat area that we were able to obtain is shown in Fig. 7(a). From the Fourier transform (inset), we obtained $d_{\text{exp}}^{(120)\text{Pt}} = 0.67(3)$ and 0.70(3) nm. For YPdBi, a large, atomically flat area is presented in Fig. 7(b). Here, the Fourier transform yielded $d_{\text{exp}}^{(120)\text{Pd}} = 0.61(3)$ and 0.72(3) nm. It is worthwhile to notice that the Fourier transforms even have a slightly rectangular shape [see also Fig. 2(i)], consistent with the asymmetry between the distance of corrugations.

APPENDIX C: REPRODUCIBILITY OF THE SPECTRA

As mentioned in Sec. II, four YPdBi and three YPtBi samples were cleaved *in situ* and subsequently investigated by STM/STS. To provide support for the reproducibility of our data, specifically the spectra, we exemplify here the results obtained on different samples of YPtBi as well as YPdBi. For comparison, we also reproduced in Fig. 8 the spectra of Fig. 3, marked S1 and S3, respectively. Clearly, the spectra of different samples of a given material compare well, and all the main features are reproduced. Most importantly for the main conclusion of our investigation, the reduction of the LDOS at E_{F} is clearly reproduced upon going from YPtBi to YPdBi.

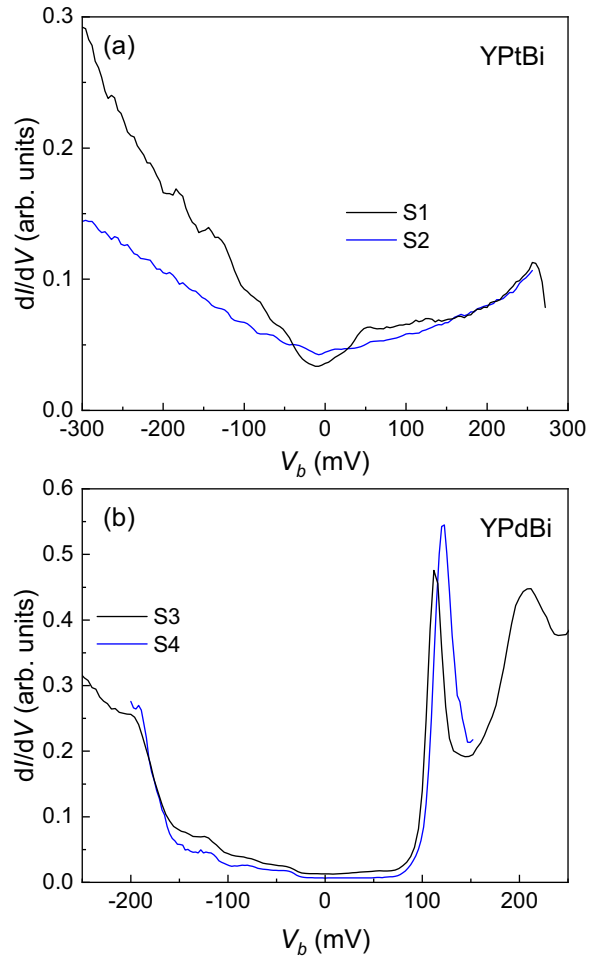

FIG. 8. Comparison of results obtained on different samples of (a) YPtBi and (b) YPdBi. Clearly, the dI/dV curves of a given material are well reproduced. All spectra are averages over certain areas; for S1 and S3 they are described in Fig. 3. The averages were taken within a 20×10 nm^2 field of view ($V_b = -300$ mV, $I_{sp} = 0.7$ nA) for spectra S2, and a 4×4 nm^2 field of view ($V_b = -200$ mV, $I_{sp} = 0.6$ nA) for S4.

APPENDIX D: DETAILS OF BULK AND SURFACE BAND-STRUCTURE CALCULATIONS

1. Bulk band-structure calculations

We were able to reproduce the bands at the Γ point using the modified Becke-Johnson (mBJ) pseudopotential, see Fig. 9, as given in [29,30]. Here, the topological properties can be described by $\Delta E = E_{\Gamma_6} - E_{\Gamma_8}$, which is negative for systems with band inversion [29] (as mentioned in the Introduction). Indeed, for YPdBi we find $\Delta E \simeq +0.35$ eV, while for YPtBi we obtain approximately -0.79 eV. In other words, our calculations specify YPtBi as a zero-gap semiconductor. Both values are similar to those reported earlier [29–31]. It is worth pointing out that even though different pseudopotentials might result in similar densities of states, some of those pseudopotentials do not reproduce correctly the band inversion [82]. Finally, these results depend strongly on the lattice constant [31].

2. Slab calculations for the (111) plane

The surface spectral functions, calculated within the Green function technique for semi-infinite systems, for the (111) surface planes of YPdBi and YPtBi are presented in Figs. 10(a) and 11(b), respectively [cf. Figs. 3(c) and 3(f) for the (120) plane]. In the case of a Bi-terminated (111) surface of YPdBi, there is no Dirac point at the $\bar{\Gamma}$ point, as expected [Fig. 10(a)]. In the YPtBi case, the Dirac point appears below the Fermi level E_{F}, as seen in Fig. 10(b). This result is consistent with previous DFT calculations and ARPES experiments [34,35]. It is worth noting that our slab calculations improve our understanding of the lack of changes in the LDOS near defects in this plane; cf. Fig. 4(e). As discussed in Sec. III D, the bulk LDOS has some impact in our data. Near E_{F}, we find trivial

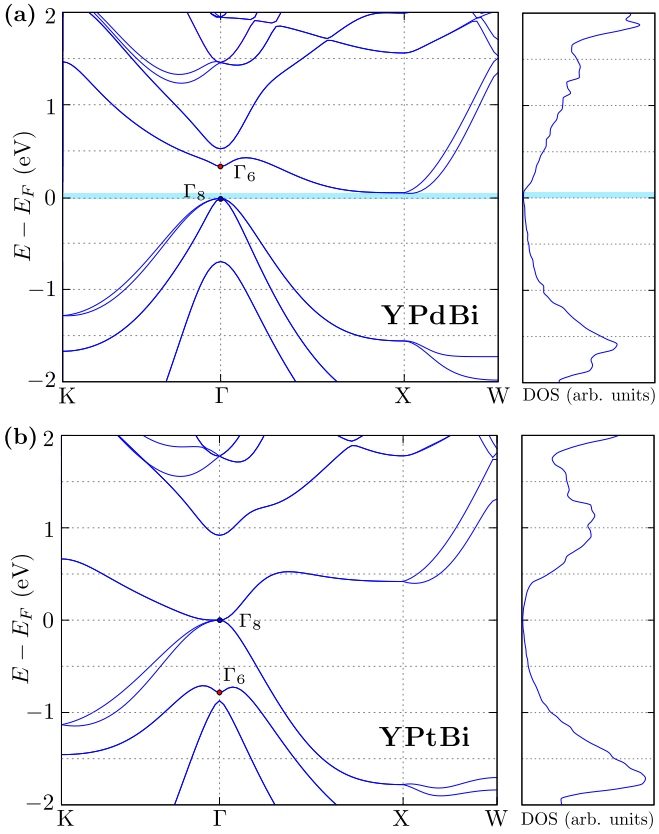

FIG. 9. Electronic band structures and density of states (DOS) for bulk (a) YPdBi and (b) YPtBi. The Γ_6 and Γ_8 bands are marked in the figure. The light-blue stripe in (a) visualizes the gap of ∼0.15 eV width.

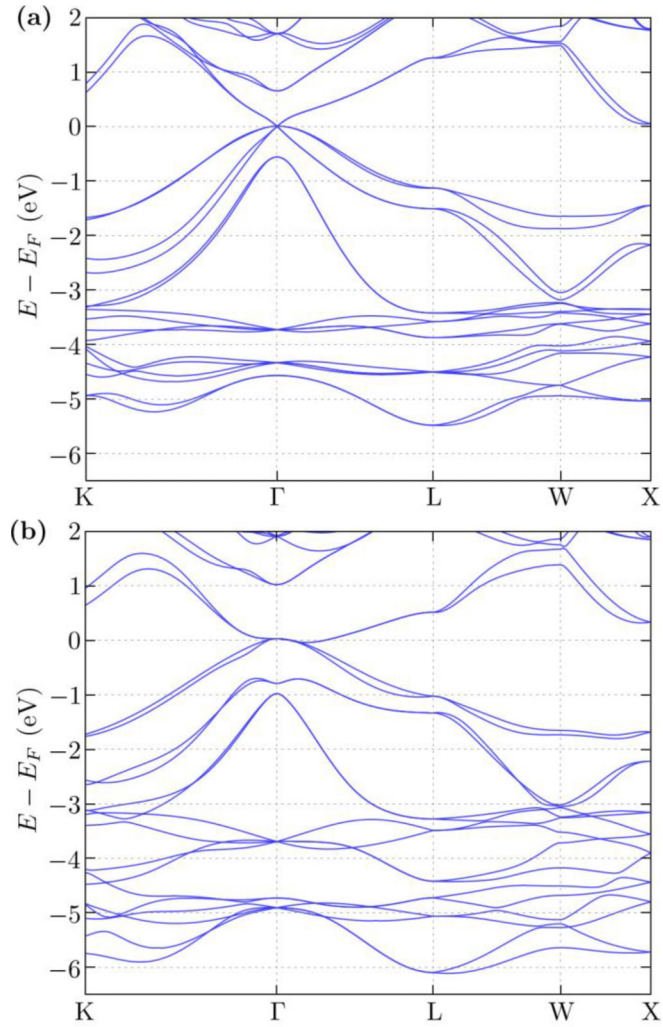

FIG. 11. The electronic band structure of (a) bulk YPdBi and (b) YPtBi obtained from DFT GGA PBE calculations.

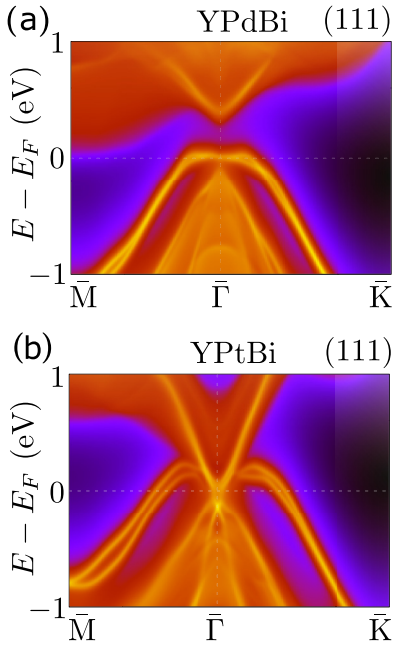

FIG. 10. Surface spectral functions of (a) YPdBi and (b) YPtBi for the (111) surface planes.

and topological bands, which may complicate the scattering process even further. Therefore, the change in the LDOS due to trivial surface states may be hard to detect within this energy window.

3. Direct slab band-structure calculations

Due to the technical limitations of the mBJ potential implemented in VASP, it cannot be used directly to study the slab band structure. As such, to present the main impact of the surface reconstruction on the electronic band structure, we performed DFT calculations using GGA with Perdew-Burke-Ernzerhof (PBE) parametrization [67]. Here, we should emphasize that this approach (DFT with GGA + PBE) does not correctly reproduce the bulk band structure of half-Heusler compounds, a problem well reported in the literature [58–60]. This is reflected in the absence of the band gap for YPdBi [cf. Figs. 9(a) and 11(a)] or incorrect band curvatures around the Γ point in the band structure of YPtBi [cf. Figs. 9(b) and 11(b)]. Nevertheless, this type of calculation can be used to present the main features of the band structure of (120) surfaces with reconstruction.

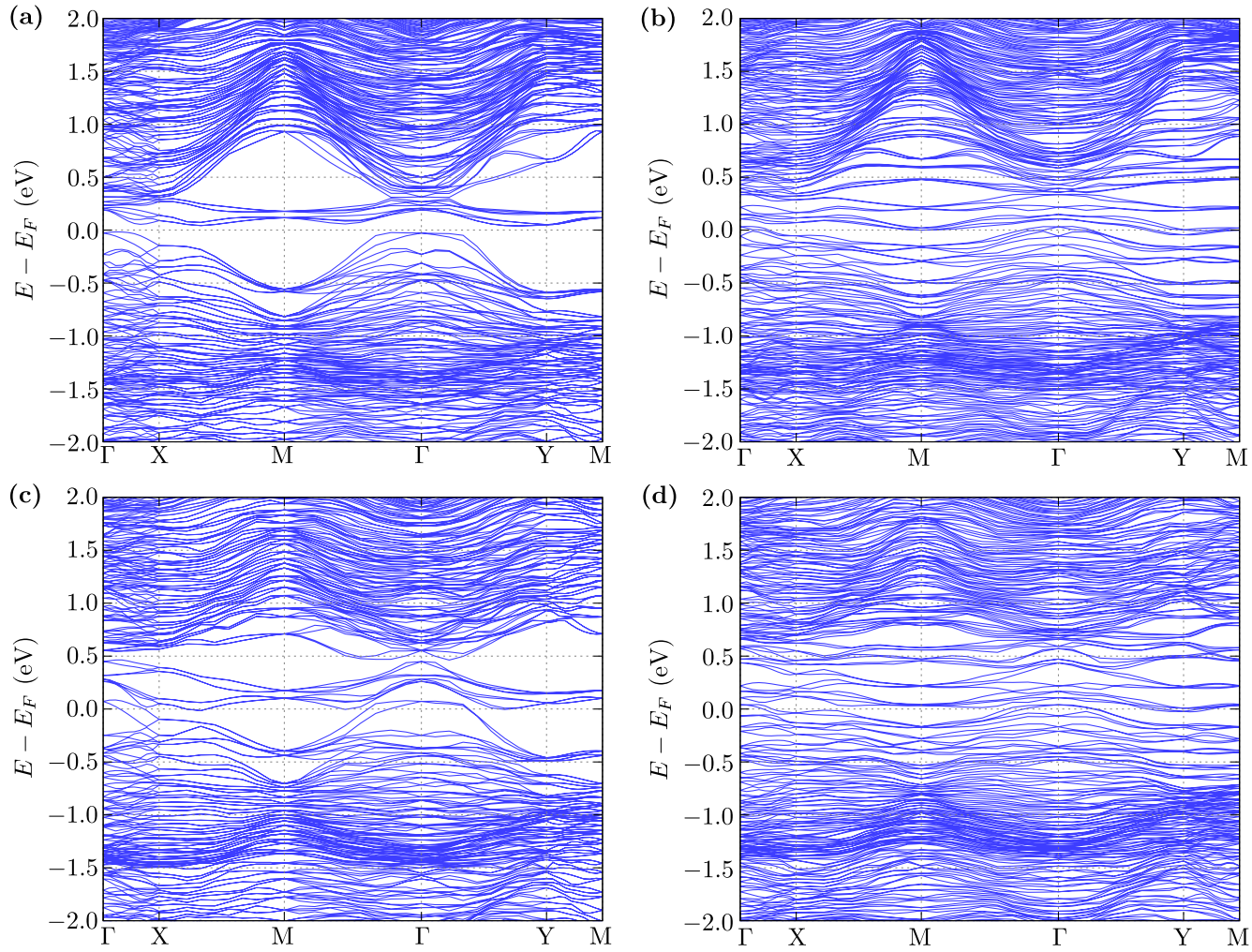

FIG. 12. The electronic band structure of slab YPdBi (top panels) and YPtBi (bottom panels) obtained from DFT GGA PBE calculations. Left and right panels correspond to the (120) surface without and with surface reconstruction, respectively.

For the simulation of the (120) surface band structure, we constructed slab models containing three layers of the discussed compounds (mostly 28 formula units). The reconstruction of the surface was introduced "by hand," i.e., by removing some atoms from the surfaces. From the self-consistently found charge distributions, the STM simulations were computed [see Figs. 2(j) and 2(k)]. Similarly, the electronic band structures for both compounds are presented in Fig. 12, where the results obtained for surfaces without and with surface reconstruction are presented on the left and right panels, respectively. For both YPdBi and YPtBi (120) surfaces without reconstruction (left panels in Fig. 12), we observed the realization of the surface states above E_F. The introduction of surface reconstructions on the (120) surface led to a multiplication of the surface states, an effect that is well visible at the M points in the right panels of Fig. 12. The additional, "extra" surface states come from the hanging (nonbonded) orbitals in the surface plane, due to the absence of some atoms on the surface (i.e., the surface reconstruction). This main feature of the band structure for the reconstructed surface, i.e., the surface states multiplication, is expected to also be present in the case of a "correctly" obtained band structure, i.e., if calculated with mBJ potential.

[1] K. v. Klitzing, G. Dorda, and M. Pepper, New method for high-accuracy determination of the fine-structure constant based on quantized Hall resistance, Phys. Rev. Lett. **45**, 494 (1980).

[2] B. A. Bernevig, T. L. Hughes, and S.-C. Zhang, Quantum spin Hall effect and topological phase transition in HgTe quantum wells, Science **314**, 1757 (2006).

[3] M. Konig, S. Wiedmann, C. Brüne, A. Roth, H. Buhmann, L. W. Molenkamp, X.-L. Qi, and S.-C. Zhang, Quantum spin Hall insulator state in HgTe quantum wells, Science **318**, 766 (2007).

[4] K. Manna, Y. Sun, L. Muechler, J. Kübler, and C. Felser, Heusler, Weyl and Berry, Nat. Rev. Mater. **3**, 244 (2018).

[5] N. P. Armitage, E. J. Mele, and A. Vishwanath, Weyl and Dirac semimetals in three-dimensional solids, Rev. Mod. Phys. **90**, 015001 (2018).

[6] M. Z. Hasan and C. L. Kane, Colloquium: Topological insulators, Rev. Mod. Phys. **82**, 3045 (2010).

[7] B. Q. Lv, T. Qian, and H. Ding, Experimental perspective on three-dimensional topological semimetals, Rev. Mod. Phys. **93**, 025002 (2021).

[8] Z. Wang, A. Alexandradinata, R. J. Cava, and B. A. Bernevig, Hourglass fermions, Nature (London) **532**, 189 (2016).

[9] S.-Y. Xu, M. Neupane, C. Liu, D. Zhang, A. Richardella, L. A. Wray, N. Alidoust, M. Leandersson, T. Balasubramanian, J. Sánchez-Barriga *et al.*, Hedgehog spin texture and Berry phase tuning in a magnetic topological insulator, Nat. Phys. **8**, 616 (2012).

[10] Y. Tokura, M. Kawasaki, and N. Nagaosa, Emergent functions of quantum materials, Nat. Phys. **13**, 1056 (2017).

[11] B. Singh, H. Lin, and A. Bansil, Topology and Symmetry in Quantum Materials, Adv. Mater. **35**, 2201058 (2023).

[12] B. Singh, H. Lin, R. Prasad, and A. Bansil, Role of surface termination in realizing well-isolated topological surface states within the bulk band gap in $TlBiSe_2$ and $TlBiTe_2$, Phys. Rev. B **93**, 085113 (2016).

[13] G. Eguchi, K. Kuroda, K. Shirai, Y. Ando, T. Shinjo, A. Kimura, and M. Shiraishi, Precise determination of two-carrier transport properties in the topological insulator $TlBiSe_2$, Phys. Rev. B **91**, 235117 (2015).

[14] S. V. Eremeev, G. Landolt, T. V. Menshchikova, B. Slomski, Y. M. Koroteev, Z. S. Aliev, M. B. Babanly, J. Henk, A. Ernst, L. Patthey *et al.*, Atom-specific spin mapping and buried topological states in a homologous series of topological insulators, Nat. Commun. **3**, 635 (2012).

[15] L. Jiao, S. Rößler, D. Kasinathan, P. F. S. Rosa, C. Guo, H. Q. Yuan, C.-X. Liu, Z. Fisk, F. Steglich, and S. Wirth, Magnetic and defect probes of the SmB_6 surface state, Sci. Adv. **4**, eaau4886 (2018).

[16] H. Pirie, Y. Liu, A. Soumyanarayanan, P. Chen, Y. He, M. M. Yee, P. F. S. Rosa, J. D. Thompson, D.-J. Kim, Z. Fisk, X. Wang, J. Paglione, D. K. Morr, M. H. Hamidian, and J. E. Hoffman, Imaging emergent heavy Dirac fermions of a topological Kondo insulator, Nat. Phys. **16**, 52 (2020).

[17] C. Guo, F. Wu, Z. Wu, M. Smidman, C. Cao, A. Bostwick, C. Jozwiak, E. Rotenberg, Y. Liu, F. Steglich *et al.*, Evidence for Weyl fermions in a canonical heavy-fermion semimetal YbPtBi, Nat. Commun. **9**, 4622 (2018).

[18] S. Dzsaber, X. Yan, M. Taupin, G. Eguchi, A. Prokofiev, T. Shiroka, P. Blaha, O. Rubel, S. E. Grefe, H.-H. Lai *et al.*, Giant spontaneous Hall effect in a nonmagnetic Weyl-Kondo semimetal, Proc. Natl. Acad. Sci. (USA) **118**, e2013386118 (2021).

[19] A. Aishwarya, Z. Cai, A. Raghavan, M. Romanelli, X. Wang, X. Li, G. Gu, M. Hirsbrunner, T. Hughes, F. Liu *et al.*, Spin-selective tunneling from nanowires of the candidate topological Kondo insulator SmB_6, Science **377**, 1218 (2022).

[20] S. Wirth and P. Schlottmann, An STM perspective on hexaborides: Surface states of the Kondo insulator SmB_6, Adv. Quantum Technol. **4**, 2100102 (2021).

[21] S. Paschen and Q. Si, Quantum phases driven by strong correlations, Nat. Rev. Phys. **3**, 9 (2021).

[22] C. Palmstrøm, Epitaxial Heusler alloys: New materials for semiconductor spintronics, MRS Bull. **28**, 725 (2003).

[23] T. Graf, C. Felser, and S. S. P. Parkin, Simple rules for the understanding of Heusler compounds, Prog. Solid State Chem. **39**, 1 (2011).

[24] W. G. Zeier, J. Schmitt, G. Hautier, U. Aydemir, Z. M. Gibbs, C. Felser, and G. J. Snyder, Engineering half-Heusler thermoelectric materials using Zintl chemistry, Nat. Rev. Mater. **1**, 16032 (2016).

[25] E. D. Mun, S. L. Bud'ko, C. Martin, H. Kim, M. A. Tanatar, J.-H. Park, T. Murphy, G. M. Schmiedeshoff, N. Dilley, R. Prozorov, and P. C. Canfield, Magnetic-field-tuned quantum criticality of the heavy-fermion system YbPtBi, Phys. Rev. B **87**, 075120 (2013).

[26] M. F. Hundley, J. D. Thompson, P. C. Canfield, and Z. Fisk, Electronic transport properties of the semimetallic heavy fermion YbBiPt, Phys. Rev. B **56**, 8098 (1997).

[27] Z. Fisk, P. C. Canfield, W. P. Beyermann, J. D. Thompson, M. F. Hundley, H. R. Ott, E. Felder, M. B. Maple, M. A. Lopez de la Torre, P. Visani, and C. L. Seaman, Massive electron state in YbBiPt, Phys. Rev. Lett. **67**, 3310 (1991).

[28] O. Eriksson, J. Wills, and A. Boring, Electronic structure of the RBiPt compounds (R = Y and Yb), J. Alloys Compd. **185**, 145 (1992).

[29] W. Feng, D. Xiao, Y. Zhang, and Y. Yao, Half-Heusler topological insulators: A first-principles study with the Tran-Blaha modified Becke-Johnson density functional, Phys. Rev. B **82**, 235121 (2010).

[30] W. Al-Sawai, H. Lin, R. S. Markiewicz, L. A. Wray, Y. Xia, S.-Y. Xu, M. Z. Hasan, and A. Bansil, Topological electronic structure in half-Heusler topological insulators, Phys. Rev. B **82**, 125208 (2010).

[31] S. Chadov, X. Qi, J. Kübler, G. H. Fecher, C. Felser, and S. C. Zhang, Tunable multifunctional topological insulators in ternary Heusler compounds, Nat. Mater. **9**, 541 (2010).

[32] H. Lin, L. A. Wray, Y. Xia, S. Xu, S. Jia, R. J. Cava, A. Bansil, and M. Z. Hasan, Half-Heusler ternary compounds as new multifunctional experimental platforms for topological quantum phenomena, Nat. Mater. **9**, 546 (2010).

[33] Z. Zhu, Y. Cheng, and U. Schwingenschlögl, Band inversion mechanism in topological insulators: A guideline for materials design, Phys. Rev. B **85**, 235401 (2012).

[34] Z. Liu, L. Yang, S.-C. Wu, C. Shekhar, J. Jiang, H. Yang, Y. Zhang, S.-K. Mo, Z. Hussain, B. Yan *et al.*, Observation of unusual topological surface states in half-Heusler compounds LnPtBi (Ln= Lu, Y), Nat. Commun. **7**, 12924 (2016).

[35] M. M. Hosen, G. Dhakal, K. Dimitri, H. Choi, F. Kabir, C. Sims, O. Pavlosiuk, P. Wiśniewski, T. Durakiewicz, J.-X. Zhu, D. Kaczorowski, and M. Neupane, Observation of Dirac state in half-Heusler material YPtBi, Sci. Rep. **10**, 12343 (2020).

[36] P. D. C. King, R. C. Hatch, M. Bianchi, R. Ovsyannikov, C. Lupulescu, G. Landolt, B. Slomski, J. H. Dil, D. Guan, J. L. Mi, E. D. L. Rienks, J. Fink, A. Lindblad, S. Svensson, S. Bao,

G. Balakrishnan, B. B. Iversen, J. Osterwalder, W. Eberhardt, F. Baumberger *et al.*, Large tunable Rashba spin splitting of a two-dimensional electron gas in Bi_2Se_3, Phys. Rev. Lett. **107**, 096802 (2011).

[37] J. Ruan, S.-K. Jian, H. Yao, H. Zhang, S.-C. Zhang, and D. Xing, Symmetry-protected ideal Weyl semimetal in HgTe-class materials, Nat. Commun. **7**, 11136 (2016).

[38] M. Hirschberger, S. Kushwaha, Z. Wang, Q. Gibson, S. Liang, C. A. Belvin, B. A. Bernevig, R. J. Cava, and N. P. Ong, The chiral anomaly and thermopower of Weyl fermions in the half-Heusler GdPtBi, Nat. Mater. **15**, 1161 (2016).

[39] C. Shekhar, N. Kumar, V. Grinenko, S. Singh, R. Sarkar, H. Luetkens, S.-C. Wu, Y. Zhang, A. C. Komarek, E. Kampert *et al.*, Anomalous Hall effect in Weyl semimetal half-Heusler compounds RPtBi (R = Gd and Nd), Proc. Natl. Acad. Sci. (USA) **115**, 9140 (2018).

[40] P. M. R. Brydon, L. Wang, M. Weinert, and D. F. Agterberg, Pairing of j = 3/2 fermions in half-Heusler superconductors, Phys. Rev. Lett. **116**, 177001 (2016).

[41] N. P. Butch, P. Syers, K. Kirshenbaum, A. P. Hope, and J. Paglione, Superconductivity in the topological semimetal YPtBi, Phys. Rev. B **84**, 220504(R) (2011).

[42] K. Gofryk, D. Kaczorowski, T. Plackowski, A. Leithe-Jasper, and Y. Grin, Magnetic and transport properties of rare-earth-based half-Heusler phases RPdBi: Prospective systems for topological quantum phenomena, Phys. Rev. B **84**, 035208 (2011).

[43] O. Pavlosiuk, D. Kaczorowski, and P. Wiśniewski, Superconductivity and Shubnikov-de Haas oscillations in the noncentrosymmetric half-Heusler compound YPtBi, Phys. Rev. B **94**, 035130 (2016).

[44] Y. Nakajima, R. Hu, K. Kirshenbaum, A. Hughes, P. Syers, X. Wang, K. Wang, R. Wang, S. R. Saha, D. Pratt *et al.*, Topological RPdBi half-Heusler semimetals: A new family of noncentrosymmetric magnetic superconductors, Sci. Adv. **1**, e1500242 (2015).

[45] H. Kim, M. A. Tanatar, H. Hodovanets, K. Wang, J. Paglione, and R. Prozorov, Campbell penetration depth in low carrier density superconductor YPtBi, Phys. Rev. B **104**, 014510 (2021).

[46] H. Kim, K. Wang, Y. Nakajima, R. Hu, S. Ziemak, P. Syers, L. Wang, H. Hodovanets, J. D. Denlinger, P. M. Brydon *et al.*, Beyond triplet: Unconventional superconductivity in a spin-3/2 topological semimetal, Sci. Adv. **4**, eaao4513 (2018).

[47] J. Kim, K. M. Fijalkowski, J. Kleinlein, C. Schumacher, A. Markou, C. Gould, S. Schreyeck, C. Felser, and L. W. Molenkamp, Molecular beam epitaxy of a half-Heusler topological superconductor candidate YPtBi, Phys. Rev. Mater. **7**, 024802 (2023).

[48] B. Nowak and D. Kaczorowski, NMR as a probe of band inversion in topologically nontrivial half-Heusler compounds, J. Phys. Chem. C **118**, 18021 (2014).

[49] X. Zhang, Z. Hou, Y. Wang, G. Xu, C. Shi, E. Liu, X. Xi, W. Wang, G. Wu, and X.-x. Zhang, NMR evidence for the topologically nontrivial nature in a family of half-Heusler compounds, Sci. Rep. **6**, 23172 (2016).

[50] G. G. Lesseux, T. M. Garitezi, P. F. S. Rosa, C. B. R. Jesus, S. B. Oseroff, J. L. Sarrao, Z. Fisk, R. R. Urbano, P. G. Pagliuso, and C. Rettori, Unusual diffusive effects on the ESR of Nd^{3+} ions in the tunable topologically nontrivial semimetal YBiPt, J. Phys.: Condens. Matter **28**, 125601 (2016).

[51] H. Baek, J. Ha, D. Zhang, B. Natarajan, J. P. Winterstein, R. Sharma, R. Hu, K. Wang, S. Ziemak, J. Paglione *et al.*, Creating nanostructured superconductors on demand by local current annealing, Phys. Rev. B **92**, 094510 (2015).

[52] J. K. Kawasaki, A. Sharan, L. I. Johansson, M. Hjort, R. Timm, B. Thiagarajan, B. D. Schultz, A. Mikkelsen, A. Janotti, and C. J. Palmstrøm, A simple electron counting model for half-Heusler surfaces, Sci. Adv. **4**, eaar5832 (2018).

[53] J. C. Souza, C. B. R. Jesus, G. G. Lesseux, P. F. S. Rosa, R. R. Urbano, and P. Pagliuso, Crystalline electric field study in a putative topologically trivial rare-earth doped YPdBi compound, J. Phys.: Condens. Matter **31**, 465701 (2019).

[54] P. E. Blöchl, Projector augmented-wave method, Phys. Rev. B **50**, 17953 (1994).

[55] G. Kresse and J. Hafner, *Ab initio* molecular-dynamics simulation of the liquid-metal–amorphous-semiconductor transition in germanium, Phys. Rev. B **49**, 14251 (1994).

[56] G. Kresse and J. Furthmüller, Efficient iterative schemes for *ab initio* total-energy calculations using a plane-wave basis set, Phys. Rev. B **54**, 11169 (1996).

[57] G. Kresse and D. Joubert, From ultrasoft pseudopotentials to the projector augmented-wave method, Phys. Rev. B **59**, 1758 (1999).

[58] A. D. Becke and E. R. Johnson, A simple effective potential for exchange, J. Chem. Phys. **124**, 221101 (2006).

[59] F. Tran and P. Blaha, Accurate band gaps of semiconductors and insulators with a semilocal exchange-correlation potential, Phys. Rev. Lett. **102**, 226401 (2009).

[60] J. A. Camargo-Martínez and R. Baquero, Performance of the modified Becke-Johnson potential for semiconductors, Phys. Rev. B **86**, 195106 (2012).

[61] H. J. Monkhorst and J. D. Pack, Special points for Brillouin-zone integrations, Phys. Rev. B **13**, 5188 (1976).

[62] M. G. Haase, T. Schmidt, C. G. Richter, H. Block, and W. Jeitschko, Equiatomic rare earth (Ln) transition metal antimonides Ln*T*Sb (*T* =Rh, Lr) and bismuthides Ln*T*Bi (*T* =Rh, Ni, Pd, Pt), J. Solid State Chem. **168**, 18 (2002).

[63] A. A. Mostofi, J. R. Yates, G. Pizzi, Y.-S. Lee, I. Souza, D. Vanderbilt, and N. Marzari, An updated version of wannier90: A tool for obtaining maximally-localised Wannier functions, Comput. Phys. Commun. **185**, 2309 (2014).

[64] G. Pizzi, V. Vitale, R. Arita, S. Blügel, F. Freimuth, G. Géranton, M. Gibertini, D. Gresch, C. Johnson, T. Koretsune, J. Ibañez-Azpiroz, H. Lee, J.-M. Lihm, D. Marchand, A. Marrazzo, Y. Mokrousov, J. I. Mustafa, Y. Nohara, Y. Nomura, L. Paulatto *et al.*, Wannier90 as a community code: new features and applications, J. Phys.: Condens. Matter **32**, 165902 (2020).

[65] Q. S. Wu, S. N. Zhang, H.-F. Song, M. Troyer, and A. A. Soluyanov, WannierTools: An open-source software package for novel topological materials, Comput. Phys. Commun. **224**, 405 (2018).

[66] J. Tersoff and D. R. Hamann, Theory of the scanning tunneling microscope, Phys. Rev. B **31**, 805 (1985).

[67] J. P. Perdew, K. Burke, and M. Ernzerhof, Generalized gradient approximation made simple, Phys. Rev. Lett. **77**, 3865 (1996).

[68] P. Bach, A. S. Bader, C. Rüster, C. Gould, C. R. Becker, G. Schmidt, L. W. Molenkamp, W. Weigand, C. Kumpf, E. Umbach, R. Urban, G. Woltersdorf, and B. Heinrich,

Molecular-beam epitaxy of the half-Heusler alloy NiMnSb on (In,Ga)As/InP (001), Appl. Phys. Lett. **83**, 521 (2003).

[69] J. K. Kawasaki, L. I. M. Johansson, B. D. Schultz, and C. J. Palmstrøm, Growth and transport properties of epitaxial lattice matched half Heusler CoTiSb/InAlAs/InP(001) heterostructures, Appl. Phys. Lett. **104**, 022109 (2014).

[70] S. J. Patel, J. K. Kawasaki, J. Logan, B. D. Schultz, J. Adell, B. Thiagarajan, A. Mikkelsen, and C. J. Palmstrøm, Surface and electronic structure of epitaxial PtLuSb (001) thin films, Appl. Phys. Lett. **104**, 201603 (2014).

[71] S. J. Patel, J. A. Logan, S. D. Harrington, B. D. Schultz, and C. J. Palmstrøm, Surface reconstructions and transport of epitaxial PtLuSb (001) thin films grown by MBE, J. Cryst. Growth **436**, 145 (2016).

[72] J. M. Tomczak, Isoelectronic tuning of heavy fermion systems: Proposal to synthesize Ce_3 Sb_4 Pd_3, Phys. Rev. B **101**, 035116 (2020).

[73] M. O. Ajeesh, S. M. Thomas, S. K. Kushwaha, E. D. Bauer, F. Ronning, J. D. Thompson, N. Harrison, and P. F. S. Rosa, Ground state of Ce_3 Bi_4 Pd_3 unraveled by hydrostatic pressure, Phys. Rev. B **106**, L161105 (2022).

[74] C. Marques, M. Bahramy, C. Trainer, I. Marković, M. D. Watson, F. Mazzola, A. Rajan, T. D. Raub, P. King, and P. Wahl, Tomographic mapping of the hidden dimension in quasiparticle interference, Nat. Commun. **12**, 6739 (2021).

[75] L. C. Rhodes, W. Osmolska, C. A. Marques, and P. Wahl, Nature of quasiparticle interference in three dimensions, Phys. Rev. B **107**, 045107 (2023).

[76] P. G. Pagliuso, C. Rettori, M. E. Torelli, G. B. Martins, Z. Fisk, J. L. Sarrao, M. F. Hundley, and S. B. Oseroff, Crystal-field study in rare-earth-doped semiconducting YBiPt, Phys. Rev. B **60**, 4176 (1999).

[77] W. Wang, Y. Du, G. Xu, X. Zhang, E. Liu, Z. Liu, Y. Shi, J. Chen, G. Wu, and X.-x. Zhang, Large linear magnetoresistance and Shubnikov-de Hass oscillations in single crystals of YPdBi Heusler topological insulators, Sci. Rep. **3**, 2181 (2013).

[78] J. C. Souza, G. G. Lesseux, R. R. Urbano, C. Rettori, and P. G. Pagliuso, Diffusive-like effects and possible non trivial local topology on the half-Heusler YPdBi compound, AIP Adv. **8**, 055713 (2018).

[79] H. Yang, J. Yu, S. S. P. Parkin, C. Felser, C.-X. Liu, and B. Yan, Prediction of triple point fermions in simple half-Heusler topological insulators, Phys. Rev. Lett. **119**, 136401 (2017).

[80] J. Xiao and B. Yan, First-principles calculations for topological quantum materials, Nat. Rev. Phys. **3**, 283 (2021).

[81] Y. Z. Zhou, J. Chen, Z. X. Li, J. Luo, J. Yang, Y. F. Guo, W. H. Wang, R. Zhou, and G. Q. Zheng, Antiferromagnetic spin fluctuations and unconventional superconductivity in topological superconductor candidate YPtBi revealed by ^{195} Pt-NMR, Phys. Rev. Lett. **130**, 266002 (2023).

[82] M. Meinert, Unconventional superconductivity in YPtBi and related topological semimetals, Phys. Rev. Lett. **116**, 137001 (2016).